JACS
JOURNAL OF THE AMERICAN CHEMICAL SOCIETY
pubs.acs.org/JACS
Article

Perpendicular Alignment of Covalent Organic Framework (COF) Pore Channels by Solvent Vapor Annealing

Congcong Yin, Ming Liu, Zhe Zhang, Mingjie Wei, Xiansong Shi, Yatao Zhang, Jingtao Wang, and Yong Wang*

Cite This: J. Am. Chem. Soc. 2023, 145, 11431−11439

ABSTRACT: Covalent organic frameworks (COFs) have showcased great potential in diverse applications such as separation and catalysis, where mass transfer confined in their pore channels plays a significant role. However, anisotropic orientation usually occurs in polycrystalline COFs, and perpendicular alignment of COF pore channels is ultimately desired to maximize their performance. Herein, we demonstrate a strategy, solvent vapor annealing, to reorient COF pore channels from anisotropic orientation to perpendicular alignment. COF thin films are first synthesized to have flexible N−H bonds in their skeletons, thus having structural mobility to enable molecular rearrangement. A solvent with low relative permittivity and a conjugated structure is then identified to have a strong affinity toward the COFs, allowing its vapor to easily penetrate into the COF interlayers. The solvent vapor weakens the $\pi-\pi$ interaction and consequently allows the COF monolayers to dissociate. The COF monolayers undergo a reorientation process that converts from random stacking into the face-on stacking fashion, in which the through COF pores are perpendicularly aligned. The aligned COF film exhibits high separation precision toward ions featuring a size difference down to 2 Å, which is 8 times higher than that of the anisotropically oriented counterpart. This work opens up an avenue for COF orientation regulation by solvent vapor annealing and reveals the essential role of the perpendicular alignment of COF pore channels to enable precision separations.

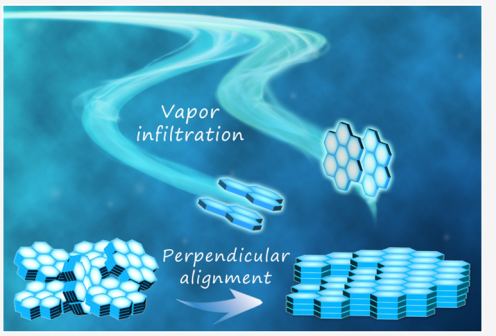

INTRODUCTION

Two-dimensional covalent organic frameworks (2D COFs) are a type of porous and crystalline framework materials which are constructed purely by organic building blocks.[1−4] They are linked by in-plane covalent bonds to form atomic-layer-thick monolayers, and the monolayers are further stacked into laminar structures driven by the out-of-plane $\pi-\pi$ interaction.[5,6] The in-plane pores of each monolayer are connected to form continuous and one-dimensional through pores along the stacking direction. Through pores in COFs possess the superiority of uniform but tunable aperture sizes typically lower than 10 nm and appreciable structural robustness. These features make COFs a highly promising platform for catalysis, separation, control release, and many other applications where the mass transfer in the confined pores plays a significant role in determining the performances.[7−11] Specifically, COF-based membranes are expected to show nanofiltration performances with high separation precision, which are thought to be superior to conventional membranes made by amorphous polymers.[12−14] However, COF crystallites tend to grow randomly, forming a polycrystalline structure with the pore channels anisotropically oriented in all directions (Figure 1a). In this regard, anisotropic orientation compromises the well-defined structures of the through pores and increases the grain boundaries that lead to defect-like intercrystalline gaps, impairing the separation precision. Therefore, COF membranes with the pore channels aligned in the perpendicular direction are of great promise because they not only maximize separation precision by minimizing the intercrystalline defects but also shorten the distance of mass transfer, favoring permeance (Figure 1b).[15−17] Nevertheless, the control on the orientation of COF pore channels appears to be overlooked, and the pore channels are usually assumed to be perpendicularly oriented, although it is not true in most cases.

The reorientation of the COF crystallites relies on the modulation of the interaction between adjacent COF layers and requires changing the stacking fashion and accordingly tuning the arrangement of these porous frameworks. This can be directly realized by using different precursors during the synthesis of COFs. Zhao et al.[18] introduced steric substituents into the precursors, synthesizing COFs with the substituents out of the plane. The arrangement of COF monolayers was changed into an inclined stacking fashion, which significantly

Received: March 28, 2023
Published: May 10, 2023

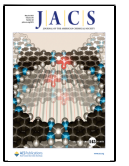

https://doi.org/10.1021/jacs.3c03198
J. Am. Chem. Soc. 2023, 145, 11431−11439

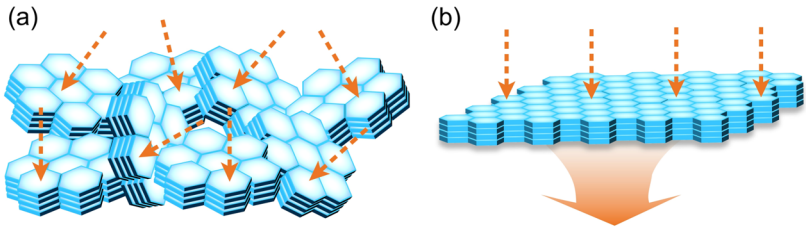

Figure 1. Schematic diagram of the (a) anisotropically oriented and (b) perpendicular aligned COF thin films.

affected the mass transport within pore channels. Bein et al.[19] utilized propeller-shaped precursors to adjust interlayer interactions, which was favorable to guide the stacking of COF layers during the nucleation and growth processes. Furthermore, the stacking fashion can be regulated by the electrostatic interaction. The COF monolayers with opposite charges and different apertures can be assembled to form interlaced pore networks, facilitating molecular transport and separation.[20] Unfortunately, COF precursors with different substituents may show considerable variance in the reaction activity and crystalline ability, and well-defined COF structures are frequently not available. Aiming to directly produce perpendicularly aligned COF nanochannels, Lai et al.[11,14] reduced the concentration of catalysts and reaction temperature, which are beneficial for the nucleation and crystallization processes. Su et al.[21] adjusted the potential difference across the interface, thus promoting the interfacial polymerization to grow oriented COF membranes. These results foreshadow that the oriented two-dimensional (2D) COF membrane may offer a distinctive platform with enhanced transport efficiency. Despite such advances, further studies are required to shorten the processing time for arranging the oriented COF nanochannels and elucidate the underlying mechanism. Moreover, control over the crystal orientation applicable to most COFs is an important aspect, which contributes to the understanding of framework assembly. The perpendicular alignment of COF nanochannels reported in previous works was realized in some specific COFs synthesized under delicately controlled conditions. The orientation mechanism within the synthetic processes largely remains unclear, which limits the number of frameworks amenable to these approaches. However, in most cases, as-synthesized COF films are in the random orientation; an additional reorientation is necessary to align the randomly oriented COF pore channels into the perpendicular orientation. Moreover, the perpendicular alignment of preformed COF films was never explored before. Therefore, it is highly desired to explore strategies to obtain perpendicularly oriented pore nanochannels from originally randomly oriented COF thin films.

Solvents play a crucial role in the synthesis of COFs, in which the characteristics of solvents (e.g., viscosity, polarity, coordination ability, etc.) notably affect the crystallization process and structural evolution.[22−24] Rational selection of solvents is significant to regulate the attractive interaction between adjacent COF layers and accordingly adjust the stacking fashion. For instance, Dichtel et al.[25] found that 2D hydrazone-linked COFs can be exfoliated into few-layer sheets after immersion in the solvent used to synthesize the COFs. The solvation effect accounts for this effect, in which the strong affinity between solvent molecules and COFs weakens the interlayer interaction. Zhao et al.[26] found that 2D COFs showed an obvious interlayer shifting when immersed in a proper solvent, leading to the stacking rearrangement of adjacent COF layers. In this context, solvated COFs experiencing weakened interactions may endow COF skeletons with structural mobility, which is conducive to orienting COFs in the desired direction. However, as the interlayer distances of COFs are in the sub-nanometer scale, it would be very difficult for solvent liquids to sufficiently penetrate into the COF interlayers. Alternatively, considering that gases show a diffusion rate two to three magnitudes higher than liquids, we expect that solvent vapors have a much stronger diffusion ability to penetrate into the COF interlayers compared to solvents in the liquid state, thus leading to more effective tuning on the interlayer interactions.[27] Also importantly, the introduction and removal of solvent vapors into and from the system containing the COF materials can be easily and rapidly operated without the tedious rinsing and drying steps required in the use of solvent liquids, which may cause structural collapse as a result of phase changes. Actually, solvent vapors have been extensively used for annealing block copolymers,[28,29] perovskites,[27,30,31] and other organic materials[32,33] to preferentially orient them in desired directions. We believe that the infiltration of solvent vapors would significantly adjust the interlayer interactions, reorienting the COF crystallites in the desired direction. Therefore, solvent vapor annealing (SVA) to perpendicularly align COFs seems to be thermodynamically and kinetically possible but, unfortunately, has so far remained unexplored.

Herein, we investigate both the thermodynamic and kinetic factors of SVA on COFs and realize the long-desired perpendicular alignment of COF films. N−H linked COFs are first synthesized to have a relatively flexible structure, thus enabling the required structural rearrangement during SVA. A solvent with low relative permittivity is identified to allow its vapor to easily penetrate into the COF interlayers and effectively weaken the $\pi-\pi$ interaction, providing COF crystallites with sufficient mobility to move. This induces the structural rearrangement of COF monolayers, favoring face-on stacking and thus forming through pores aligned in the perpendicular direction. Thus-aligned COF thin films exhibit impressive sieving precision toward ions with a size difference down to 2 Å.

RESULTS AND DISCUSSION

Synthesis of Amine-Linked TbHz Thin Films. SVA requires the material to be annealed to have certain structural flexibility or mobility to allow segments or the whole molecule to move, thus changing their configuration and orientation. However, typical COFs such as the extensively studied imine-linked ones have highly rigid skeletons with very limited segmental mobility, thus thermodynamically prohibiting reorientation by SVA. To realize a perpendicular alignment, one should first overcome the thermodynamic limit by

https://doi.org/10.1021/jacs.3c03198
J. Am. Chem. Soc. 2023, 145, 11431−11439

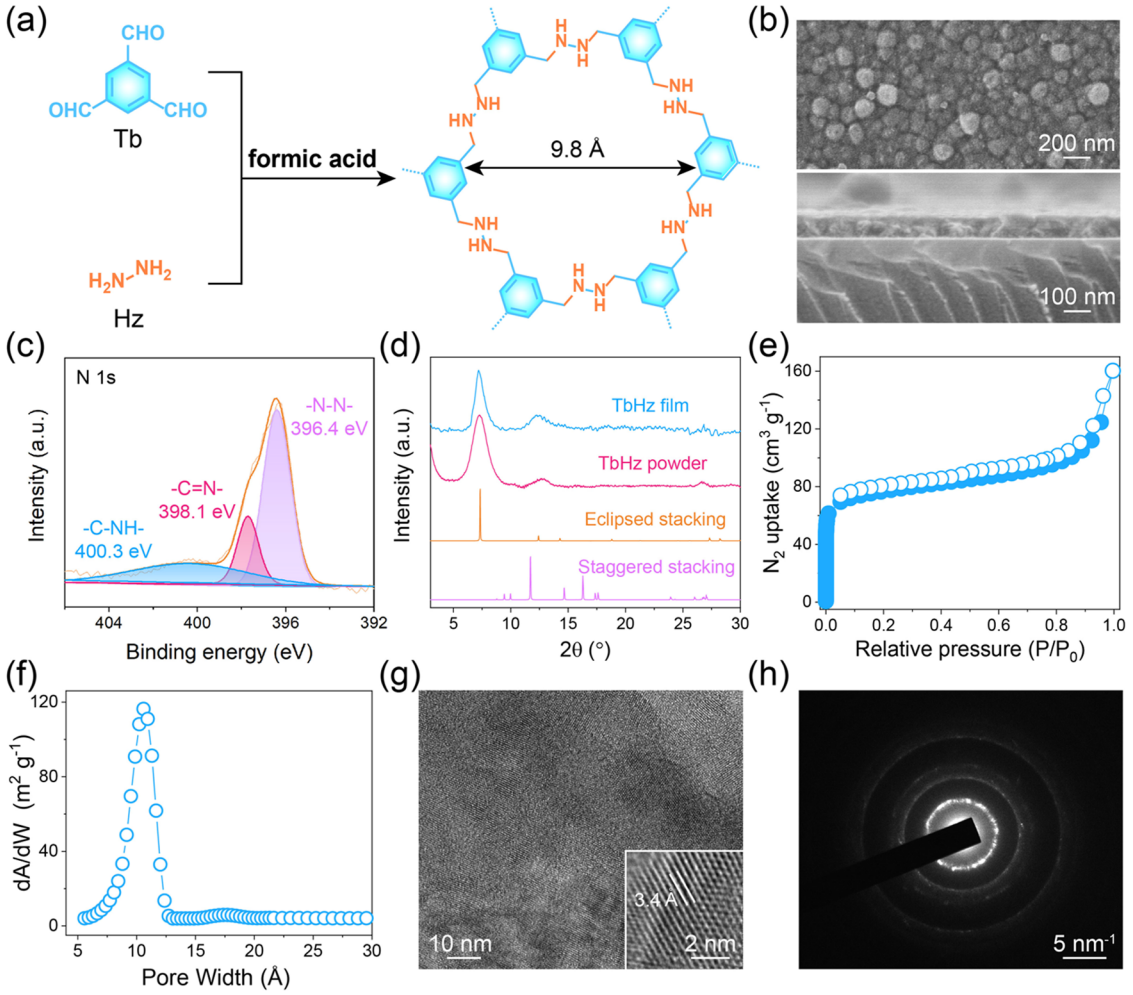

Figure 2. Synthesis of amine-linked TbHz thin films. (a) Synthetic scheme. (b) Surface (up) and cross-sectional (down) SEM images. (c) High-resolution XPS N 1s analysis. (d) Experimental XRD patterns of TbHz thin films and powders and the simulated XRD patterns of TbHz crystallites. (e) N_2 sorption isotherm curve and (f) the corresponding pore size distribution. (g) HRTEM image. Inset: the corresponding lattice distance. (h) SAED pattern.

rendering sufficient structural flexibility to COFs. We notice that amine linkages possess appreciable flexibility and can be obtained by reducing rigid imine bonds via the Eschweiler–Clarke reaction.[34] Accordingly, we synthesized flexible amine-linked COF films by covalently linking triformylbenzene (Tb) and hydrazine hydrate (Hz) (Figure 2a). Formic acid serves as both the catalyst and reducing agent, condensing the individual steps into a single one-pot crystallization–reduction process. With the process of nucleophilic additive elimination, the primary amine is *N*-methylated with the aldehyde group with the assistance of formic acid, giving iminium intermediate species and final amine products (Figure S2).[34] The film thickness can be finely tuned from ∼50 to 120 nm with a growth rate of 16 nm day^{-1} during the first 7 days (Figures 2b and S3). The yield of TbHz films (film mass divided by the total mass of monomers) increases from 3.9 to 7.2 wt % within this period. Note that the yield is comparable with the COF films prepared in other works,[35] and can be increased simply by putting more substrates in the reaction autoclave. Top-view scanning electron microscopy (SEM) images reveal the compact and cohesive morphologies of the synthesized films (Figures 2b and S4). The TbHz crystallites grow and merge together with many node-shaped regions, which is also demonstrated by the increase of surface roughness after prolonging synthesis durations (Figure S5). The formation of amine bonds in the film is confirmed by Fourier transform infrared (FTIR) and X-ray photoelectron spectroscopy (XPS) characterizations. Prolonging the reaction duration, the stretching vibration peak assigned to C–N at 1263 cm^{-1} appears and is intensified, while the peak of C=N at 1626 cm^{-1} is gradually decreased (Figure S6). In the N 1s spectra of XPS, a new peak at 400.3 eV is observed, which is assigned to C–NH, and the reduction yield can be estimated to be 63% after synthesis for 7 days (Figures 2c and S7). These results demonstrate that TbHz films with flexible amine bonds were successfully synthesized.

As shown in Figures 2d and S8, the X-ray diffraction (XRD) pattern of the TbHz films agrees well with that of the solvothermally synthesized TbHz powders, indicating the high crystallinity of the films. Moreover, the comparison of the experimental and simulated XRD profiles suggests the eclipsed stacking of the TbHz monolayers in the films. N_2 sorption isotherms were acquired at 77 K to estimate the porosity and pore size distribution of the film via the Brunauer–Emmett–Teller (BET) analyses (Figure 2e). The film has a typical type I isotherm curve with a sharp uptake under P/P_0 = 0.05 as a result of the presence of micropores. The pore width calculated from the nonlocal density functional theory (NLDFT) is

https://doi.org/10.1021/jacs.3c03198
J. Am. Chem. Soc. 2023, 145, 11431–11439

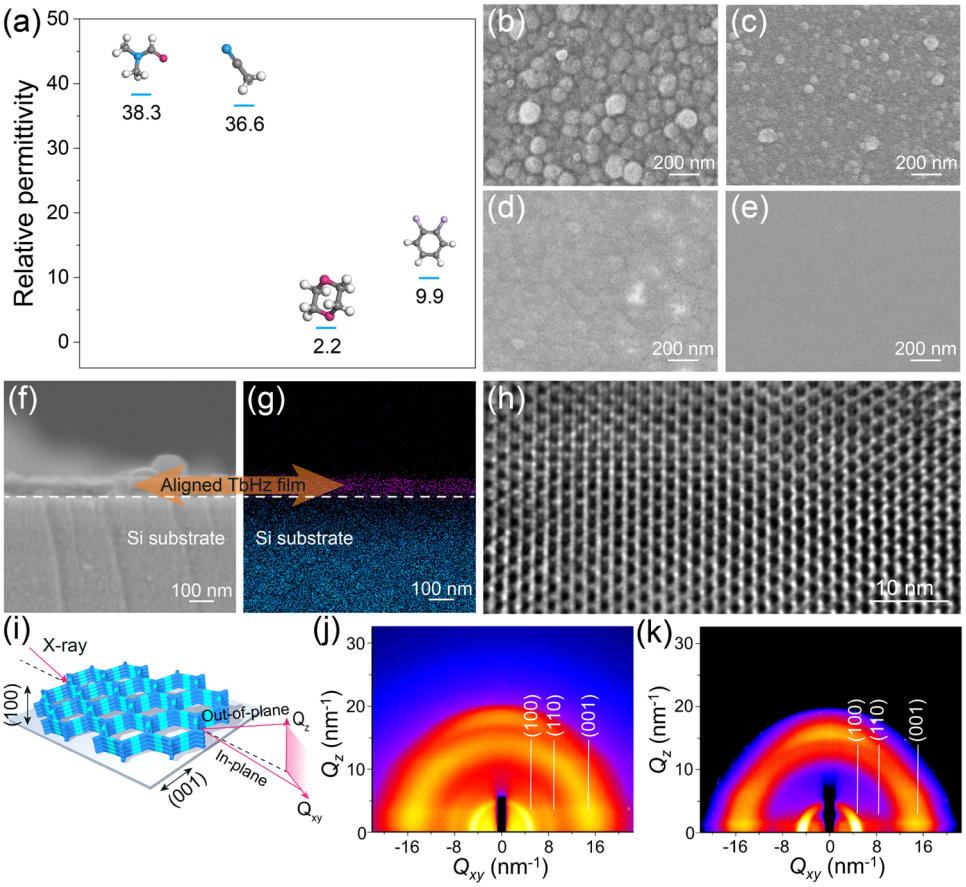

Figure 3. Solvent vapor annealing of the TbHz films. (a) Comparison of the relative permittivity of different solvents. Surface SEM images of the TbHz film annealed in (b) DMF, (c) acetonitrile (ACN), (d) 1,4-dioxane (DOX), and (e) *o*-DCB at 120 °C for 5 h. (f) Cross-sectional SEM image and (g) EDS mapping with elemental distributions of the TbHz film annealed in *o*-DCB. (h) HRTEM image of the TbHz film annealed in *o*-DCB for 5 h showing perpendicularly aligned, hexagonally arranged pores. (i) Schematic representation of the GIWAXS measurement protocol. (j, k) 2D GIWAXS patterns of the TbHz film (j) before and (k) after annealing in *o*-DCB.

centered at 10.3 Å (Figure 2f), which is slightly larger than the film linked by imine bonds (Figure S9). This could be attributed to the stretching of the flexible amine bond, thus leading to a relaxed framework. High-resolution transmission electron microscopy (HRTEM) clearly shows the lattice fringes of the film with a spacing of ~3.4 Å, which represents that the interlayer distance of TbHz monolayers originated from the $\pi-\pi$ stacking (Figures 2g and S10). Besides, clear diffraction rings also can be seen in the selected area electron diffraction (SAED) pattern, further indicating the high crystallinity and anisotropic orientation of the TbHz films (Figures 2h and S10).

Perpendicular Alignment of TbHz Thin Films by SVA. Flexible amine links thermodynamically enable SVA to reorient COFs, and there is still a kinetic issue in identifying suitable solvents to practically start and regulate the SVA process. To study the influence of solvent vapors on structural development during SVA, we screened solvents to identify the optimal condition for a perpendicular alignment (Figure 3a). We selected common solvents used in the synthesis of COFs with a permittivity gradient ranging from *N*,*N*-dimethylformamide (DMF) (38.3) to 1,4-dioxane (DOX) (2.2).[36] For these experiments, the TbHz thin films grown on the Si/SiO_2 substrates were placed in a sealed vapor chamber containing the respective solvent (Figure S1). The morphology evolution of the films was first analyzed. As shown in Figure 3b–e, crystallite assembled morphology with an obvious grain boundary can be observed after DMF annealing, which is close to that of the pristine film. Strikingly, reducing the permittivity, the films exhibited a progressively smoothening surface morphology. It is worth noting that the COF film annealed in 1, 2-dichlorobenzene (*o*-DCB) exhibits the smoothest morphology. This remarkable transformation is mainly attributed to the nonpolar and conjugated interaction between *o*-DCB vapor and TbHz, strengthening their affinity and promoting the diffusion of *o*-DCB vapor. To obtain deep insights into the strong impact of *o*-DCB vapor on the structure of the TbHz films, a time-dependent morphology analysis was conducted (Figures S11 and S12). With time elapsed, *o*-DCB vapor continuously diffuses into the crystallites, resulting in attenuated interlayer interactions and a relaxed structure. The crystallites are reorganized laterally to assemble into a uniform morphology structure after annealing for 5 h. As SVA further proceeds, the crystallites would dissociate owing to the overlong interaction between *o*-DCB vapor and TbHz, which is responsible for the presence of cracks (Figure S11g,h). Moreover, the TbHz film annealed in *o*-DCB exhibits reduced surface roughness of 4 nm, whereas that of the as-synthesized film without annealing is above 38 nm (Figures S5 and S13). This further demonstrates the structural rearrangement of COF crystallites. Energy-dispersive X-ray spectroscopy (EDS) reveals a sharp transition of the

https://doi.org/10.1021/jacs.3c03198
J. Am. Chem. Soc. 2023, 145, 11431−11439

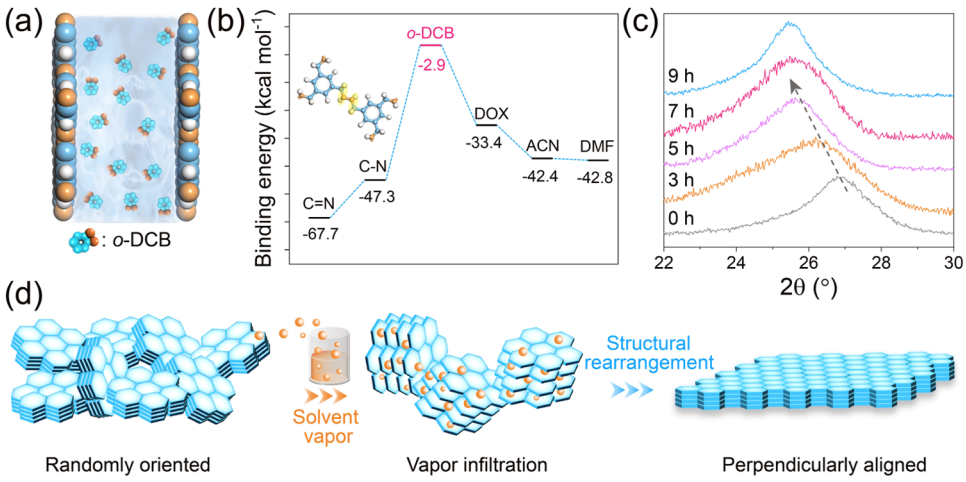

Figure 4. Perpendicular alignment of TbHz thin films. (a) Schematic simulation of the SVA process in *o*-DCB. (b) Influence of representative structures and solvent molecules on their binding energies with TbHz monolayers. The inset is the structural unit of TbHz. (c) PXRD patterns of TbHz with different durations of SVA. (d) Schematic showing the effect of infiltrating *o*-DCB vapors into the TbHz crystallites and the structural rearrangement from randomly oriented intergrown crystallites to perpendicularly aligned thin films.

TbHz film after *o*-DCB annealing, revealing that the annealed TbHz film possesses a uniform morphology across the thickness (Figure 3f,g). The ratio of the C−NH bond is kept at ∼65% with the extension of annealing duration, which reflects the framework integrity during SVA (Figure S14). FTIR characterization reveals that the relative intensity of the C═O bond decreases with the extension of annealing duration, demonstrating the occurrence of the Schiff base reaction (Figure S15). In addition, the crystallinity of TbHz films is slightly enhanced with the extension of the annealing duration, implying that recrystallization takes place during the SVA process (Figure S16).

The preferential orientation of the *o*-DCB-annealed TbHz films was visualized with HRTEM and corresponding SAED patterns. With an SVA duration of 3 h, the TbHz film shows randomly oriented pores with lattice distortion, indicating the mobility of the segments during SVA (Figure S17). After prolonging the SVA process to 5 h, the star-shaped contrasts surrounded by dark contours are clearly detected in a large size, where the darkest parts represent the hexagonal pore channels in the TbHz film along the [001] direction (Figures 3h, S18 and S19). The lateral lattice size reflects a pore diameter of approximately 9.1 Å for the annealed TbHz film, which corresponds well to the theoretical upper diameter of 9.8 Å (Figure 2a). This suggests that the thus-annealed TbHz film has a face-on orientation and extends horizontally. The SAED pattern reveals the diffraction dots cohering along the lattice direction, demonstrating the perpendicular alignment of the film (Figure S19). The observation of the lattice evolution indicates that SVA is favorable for crystallite relaxation, which affects the local structures at grain boundaries. As a result, this rearrangement process could promote the coalescence of adjacent domains, affording the large-area aligned structures.

To further understand the degrees of orientation on a macroscopic scale, grazing-incidence wide-angle X-ray scattering (GIWAXS) was performed (Figure 3i). The 2D area detector is used to simultaneously acquire the signal collection in both the in-plane and out-of-plane directions. For the pristine TbHz film, the GIWAXS pattern shows sharp reflections in both the in-plane and out-of-plane directions, reflecting the high overall crystallinity of the film over the size of several square centimeters. The well-defined and arc-like diffraction peaks at 5.3, 8.7, and 15.8 nm^{-1} are assigned to (100), (110), and (001) peaks observed in the GIWAXS pattern (Figure 3j). After annealing, the near-isotropic diffraction rings in the GIWAXS pattern of the TbHz film are replaced with discrete Bragg spots, indicating the development of a distinct preferential orientation (Figure 3k). The partial pole figure of the (100) reflection of the annealed TbHz film records its intensity as a function of the azimuthal angle. As a result, the intensity distribution narrows and intensifies, confirming that SVA enhances the face-on orientation (Figure S20). Moreover, the $\pi-\pi$ stacking signal of the annealed TbHz film is stronger than that of the pristine one, further indicative of the face-on stacking of the TbHz monolayers. To quantify the extent of the preferential orientation, we calculate the Hermans orientation factor of the (100) and (001) reflections. After annealing the TbHz film in a saturated atmosphere of *o*-DCB vapor at 120 °C for 5 h, the film gives an enhanced Hermans orientation factor of the (100) reflection from 0.12 to 0.91. Furthermore, the Hermans orientation factor of the (001) reflection also increases from 0.18 to 0.82. This enhanced orientation factor confirms that SVA not only improves the arrangement of the TbHz skeleton but also corrects the adjacent crystallites into larger crystalline domains. That is, the TbHz film with a thickness down to 100 nm annealed in *o*-DCB possesses ordered pore channels that are perpendicularly aligned and spanned the entire thickness.

Structural Evolution in the Annealing of TbHz Films. To understand to what extent the molecular factors could influence the evolution of TbHz films during SVA, we performed molecular dynamics (MD) simulations to study the interactions between interlayers and various solvents (Figure 4a). We built an all-atom model of TbHz monolayers, which was exposed in different solvents and equilibrated for 10 ns at T = 120 °C.

In general, the flexibility of the TbHz skeleton is mainly caused by the rotation and torsion of the amine linkages, which would contribute to the structural variation during solvent annealing. Thus, we first determined the stacking interactions of the amine- and imine-linked TbHz monolayers (Figure 4b). The binding energy between the amine-linked monolayers

https://doi.org/10.1021/jacs.3c03198
J. Am. Chem. Soc. 2023, 145, 11431−11439

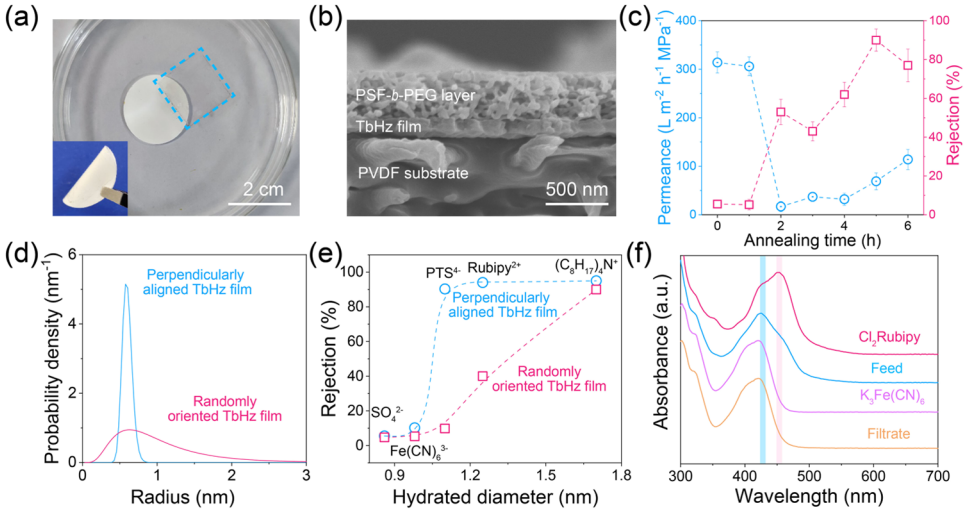

Figure 5. Composite membranes with aligned TbHz films as the selective layers. (a) Photographs of the perpendicularly aligned film protected by the PSF-*b*-PEG layer floating on water and composited with the PVDF substrate. (b) Cross-sectional SEM image of the trilayered composite structure containing the perforated PSF-*b*-PEG protective layer, the perpendicularly aligned TbHz film, and the PVDF substrate. (c) Permeance and rejection to Na_4PTS of TbHz films subjected to annealing in *o*-DCB for different durations. (d) Pore size distribution and (e) size-selective solute rejection curves of the pristine (randomly oriented) and perpendicularly aligned TbHz films. (f) UV−vis spectra of the solutions involved in the selective removal of $K_3Fe(CN)_6$ from a Cl_2Rubipy and $K_3Fe(CN)_6$ mixture using the aligned TbHz film.

(−47.3 kcal mol^{-1}) is much lower than that between the imine-linked monolayers (−67.7 kcal mol^{-1}) (Figure S21). This underlines that the amine-linked TbHz monolayers would be much more easily dissociated, which could combine more solvent molecules during SVA.

Subsequently, the interactions of TbHz monolayers within different solvent environments were examined. The *o*-DCB molecules significantly increase the stacking distance and cause the TbHz skeleton to twist relative to each other (Figures S22 and S23). This weakens the $\pi-\pi$ interaction, and the binding energy is calculated to be −2.9 kcal mol^{-1}. The value is 2−20 times lower than that in DOX, ACN, and DMF (Figures 4b and S24). Thus, the amine-linked TbHz monolayers can be readily dissociated by *o*-DCB due to the strong solvophilic effect (Figure S25), which is also experimentally confirmed in Figure 3a−e. Indeed, we experimentally detected a shift of the (001) reflection toward a lower 2θ value, corresponding to an increased stacking distance of the adjacent TbHz layers upon vapor exposure (Figures 4c and S16). This observation points to a slow anisotropic displacement of the TbHz layers promoted by the weakening of the stacking interactions, thus allowing efficient rearrangement and extension of TbHz crystallites.

To obtain the preferential orientation of TbHz pore channels during SVA, model calculations with face-on and edge-on orientations were investigated. As shown in Figure S26, perpendicularly aligning the TbHz monolayers minimizes the stacking interaction, which indicates that the face-on arrangement is the most probable conformation for stacked monolayers. Moreover, the time-depended MD simulation shows lower interaction energy between TbHz monolayers in the eclipsed stacking mode (Figure S27). These results underline that the specific interactions of *o*-DCB with the TbHz skeleton can greatly dissociate the monolayers and promote structural transformation, which contributes to the oriented alignment of TbHz crystallites.

Based on the above experimental and theoretical investigations, we understand the mechanism for the perpendicular alignment of TbHz films by SVA (Figure 4d). Amine linkages in TbHz endow the framework with flexibility and reduced interlayer interactions. *o*-DCB vapor has a favorable affinity to the flexible TbHz skeleton because of its low relative permittivity and conjugated structure. This is helpful for solvent molecules diffusing into the TbHz crystallites. In this case, the surrounded *o*-DCB further weakens $\pi-\pi$ interactions, enlarging the interlayer distance and allowing the TbHz monolayers to dissociate. Benefiting from the strong interaction between *o*-DCB molecules and TbHz monolayers, the dissociated crystallites can keep in a stable state without agglomeration. Moreover, *o*-DCB provides efficient mobility for TbHz crystallites to reorient and adopt its face-on orientation, which is thermodynamically favorable. With the evaporation of *o*-DCB, the rearranged TbHz crystallites are frozen because of the reduced mobility of the monolayers, leading to perpendicularly aligned pore channels in the TbHz films.

To demonstrate the universality of the SVA strategy, we prepared another two types of COF films: COF-LZU1 and TpPa (Figure S28). COF-LZU1 was prepared by employing Pa to replace HZ and Tb as the building blocks. As expected, COF-LZU1 films are composed of amine linkages owing to the Eschweiler−Clarke reaction of formic acid (Figure S29). SEM images exhibit the smooth morphology of the COF-LZU1 film after being annealed in o-DCB for 5 h, reflecting the structural rearrangement of COF-LZU1 crystallites (Figure S30). Meanwhile, the discrete Bragg spots can be clearly observed within the COF-LZU1 film, indicating the in-plane orientation of COF-LZU1 films after annealing (Figure S31). Conversely, obvious grain boundaries can still be observed within TpPa films after annealing for 8 h, which is mainly attributed to β-ketoenamine, which greatly restricts the structural evolution during SVA. Therefore, the SVA strategy proposed in this work is expected to be applicable to the imine-linked COFs, which have been widely studied and used in diverse applications.

Precise Separation of Perpendicularly Aligned TbHz Films. Because of the ultrathin thickness of the TbHz films, we

https://doi.org/10.1021/jacs.3c03198
J. Am. Chem. Soc. 2023, 145, 11431−11439

used a perforated polymer-assisted transfer method to protect them during the transfer operations (Figure 5a).[37,38] The polysulfone-*block*-poly(ethylene glycol) (PSF-*b*-PEG) protective layer was cavitated by selective swelling in a solvent mixture,[39] producing interconnected mesopores throughout the entire thickness with a thickness of ~400 nm (Figure S32). The copolymer-protected TbHz films were then transferred onto poly(vinylidene fluoride) (PVDF) macroporous substrates to prepare composite membranes with the TbHz films as the selective layers. Figure 5b exhibits the trilayered structure of the composite membranes, where the TbHz films as the interlayers can be clearly recognized. The copolymer-protected TbHz films are closely adhered with the underlying macroporous PVDF substrates, demonstrating good interfacial stability even under bending.

We first measured permeances and rejection properties of the composite membranes with TbHz films subjected to annealing in *o*-DCB for different durations using pyrenetetrasulfonic acid tetrasodium (Na_4PTS) with a diameter of 1.05 nm as the probe (Figure 5c). In the SVA process, the control over the annealing duration is critical as SVA effectively weakens the stacking interactions, triggering the structural rearrangement and oriented configuration. Here, the pristine TbHz films before SVA exhibit a high permeance of 314 L m^{-2} h^{-1} MPa^{-1}, but the rejection to PTS^{4-} remains at a low level of 5%. The permeance is gradually decreased to 306, 37, and 69 L m^{-2} h^{-1} MPa^{-1} after annealing in *o*-DCB for 1, 3, and 5 h, respectively. The rejections to PTS^{4-} are sharply increased from 5 to 90%. Moreover, a slight decline in the rejection is observed when the annealing duration keeps rising to 6 h. This is mainly due to the excessive interaction between *o*-DCB and TbHz monolayers, leading to cracks in the TbHz films (Figure S11). Notably, the highest rejection is obtained from the TbHz films subjected to SVA for 5 h because of their perpendicularly aligned pore channels. In addition, the aligned TbHz membranes exhibit a high ionic rejection rate and decent water permeability (Figures S33 and Table S1). Notably, the water permeability of the aligned TbHz film is comparable or even higher than that of the polyamide membranes,[40,41] which can be further enhanced by reducing the film thickness.

Solute rejection tests were performed to elucidate the precise sieving ability of the perpendicularly aligned TbHz film. The film was first challenged with poly(ethylene glycol) (PEG) of varying molar masses. The rejection data for PEG is collectively fit using a logistic function to afford a reasonable representation of the rejection characteristics of the film (Figure S34). On this basis, we estimated that the aligned TbHz film can completely reject PEG with a diameter of 1.1 nm (Figure 5d). Moreover, the narrow pore radius distribution demonstrates the highly ordered perpendicular channels of the aligned TbHz film. By contrast, the effective pore size distribution of the pristine, randomly oriented TbHz film before annealing is markedly higher, suggesting the broad distribution of the transport channels. The ionic sieving properties were evaluated using a series of ions with sizes ranging from 0.86 to 1.73 nm, viz., Na_2SO_4, $K_3Fe(CN)_6$, Na_4PTS, ruthenium tris(2,2′-bipyridyl) dichloride ($Cl_2Rubipy$), and tetra-n-octylammonium bromide ($(C_8H_{17})_4NBr$) (Figures 5e and S35).[42] For the aligned TbHz, rejection for SO_4^{2-} is lower than 10%; however, its rejection sharply increases for ions with a diameter close to 1.1 nm (90% for PTS^{4-} and 94% for $Rubipy^{2+}$). However, the pristine TbHz film exhibits a low ion rejection of 9.8% and 45% for PTS^{4-} and $Rubipy^{2+}$, respectively. The difference in solute rejections is owing to the discrepancy of the transport pathways. For the perpendicularly aligned TbHz film, transport occurs through its intrinsic channels, exhibiting precise ionic discrimination. Conversely, the pristine TbHz film with randomly oriented pore channels allows the solute to transport through both the intrinsic pores and gaps among the crystallites. As such, although the geometric-mean diameter for a solute may exceed the pore size, the passage of the solute may still occur if its dimension does not exceed the gaps among crystallites.[43,44] Besides, the TbHz films annealed in the solvents with high permittivity were also prepared with the perforated polymer-assisted transfer method (Figure S36). They display analogously inferior sieving performance, demonstrating the randomly arranged crystallites within the films (Figure S37). The above results unambiguously reveal the importance of controlling the orientation of pore channels in COF membranes for precise sieving.

Benefiting from the perpendicularly aligned nanochannels in COF membranes, we expect that the ions with similar sizes can be separated at the Angstrom scale. The essential role of the perpendicular alignment for the precise separation is further demonstrated by comparing the separation factors of different TbHz films toward similarly sized solutes, Na_2SO_4 and Na_4PTS (Figure S38). High-precision separation for Na_4PTS and Na_2SO_4 is of significance for the real-world manufacturing process. During the synthesis of Na_4PTS, which is an extensively used fluorescent material, excess H_2SO_4 is usually served as the sulfonating agent to enhance the efficiency.[45,46] However, after the reaction, the separation between Na_4PTS and H_2SO_4 with common strategies remains challenging. Precise separation offered by the perpendicularly aligned TbHz membranes is expected to improve the yield and purity of Na_4PTS. The perpendicularly aligned TbHz film exhibits the highest separator factor of 16.8, much higher than that of the randomly oriented imine-linked (7.3) and amine-linked (2.1) film. This enhancement originates from the perpendicularly aligned and ordered pore channels within the annealed TbHz film, endowing the film with superior selectivity properties. Meanwhile, the films without annealing produce higher permeance, which is mainly attributed to the additional pathways from intercrystalline gaps. The perpendicularly aligned film was then used to filter a mixture containing $K_3Fe(CN)_6$ and $Cl_2Rubipy$ to verify the ionic sieving effect. As can be seen in Figures 5f and S39, the film selectively allows the transport of $K_3Fe(CN)_6$ from the mixture, which is also confirmed by the UV−vis spectra. Furthermore, the performance stability of the aligned film was also verified over time, and there was no obvious decline in permeance and rejection (Figure S40). Hence, the SVA approach developed in this work can efficiently regulate the orientation and consequently enhance the separation precision of TbHz films, which would be significantly beneficial for improving the practical application of COF-based membranes.

CONCLUSIONS

In conclusion, we realize perpendicular alignment of COF thin films, which are strongly desired in mass-transfer-involved processes by a simple strategy of solvent vapor annealing. The COF films with flexible amine linkages possess lower interlayer binding energy, thermodynamically enabling SVA to reorient the films. *o*-DCB vapor with low permittivity and a conjugated structure exhibits considerable affinity to the nonpolar COF

https://doi.org/10.1021/jacs.3c03198
J. Am. Chem. Soc. 2023, 145, 11431−11439

skeleton, kinetically providing sufficient mobility for the crystallites to reorganize into the more favored face-on orientation. The resulting COF films present hexagonally arranged pore channels aligned along the [001] direction, which contributes to narrowed pore size distribution and precise ionic discrimination at the Angstrom precision. This work demonstrates the capability of SVA to regulate the orientation of COF thin films and reveals the decisive role of structural flexibility and the solvent−COF interactions in achieving a perpendicular alignment.

■ ASSOCIATED CONTENT

Supporting Information

The Supporting Information is available free of charge at https://pubs.acs.org/doi/10.1021/jacs.3c03198.

Experimental details; schematic and digital photos; SEM images; FTIR spectra; N_2 adsorption test; AFM images; XPS spectra; XRD patterns; HRTEM images; SAED patterns; GIWAXS pattern; simulated structures and results; performance comparison; PEG rejections; molecular sizes; ionic separation effect; and precise sieving and performance stability (PDF)

■ AUTHOR INFORMATION

Corresponding Author

Yong Wang − *State Key Laboratory of Materials-Oriented Chemical Engineering, College of Chemical Engineering, Nanjing Tech University, Nanjing 211816 Jiangsu, P. R. China; School of Energy and Environment, Southeast University, Nanjing 210096 Jiangsu, P. R. China;* orcid.org/0000-0002-8653-514X; Email: yongwang@njtech.edu.cn

Authors

Congcong Yin − *State Key Laboratory of Materials-Oriented Chemical Engineering, College of Chemical Engineering, Nanjing Tech University, Nanjing 211816 Jiangsu, P. R. China; School of Energy and Environment, Southeast University, Nanjing 210096 Jiangsu, P. R. China*

Ming Liu − *State Key Laboratory of Materials-Oriented Chemical Engineering, College of Chemical Engineering, Nanjing Tech University, Nanjing 211816 Jiangsu, P. R. China*

Zhe Zhang − *State Key Laboratory of Materials-Oriented Chemical Engineering, College of Chemical Engineering, Nanjing Tech University, Nanjing 211816 Jiangsu, P. R. China*

Mingjie Wei − *State Key Laboratory of Materials-Oriented Chemical Engineering, College of Chemical Engineering, Nanjing Tech University, Nanjing 211816 Jiangsu, P. R. China;* orcid.org/0000-0001-7601-4749

Xiansong Shi − *State Key Laboratory of Materials-Oriented Chemical Engineering, College of Chemical Engineering, Nanjing Tech University, Nanjing 211816 Jiangsu, P. R. China;* orcid.org/0000-0002-4258-7941

Yatao Zhang − *School of Chemical Engineering, Zhengzhou University, Zhengzhou 450001 Henan, P. R. China;* orcid.org/0000-0002-6832-3127

Jingtao Wang − *School of Chemical Engineering, Zhengzhou University, Zhengzhou 450001 Henan, P. R. China;* orcid.org/0000-0002-2004-9640

Complete contact information is available at: https://pubs.acs.org/10.1021/jacs.3c03198

Notes

The authors declare no competing financial interest.

■ ACKNOWLEDGMENTS

This work was financially supported by the National Natural Science Foundation of China (21825803).

■ REFERENCES

(1) Mu, Z.; Zhu, Y.; Li, B.; Dong, A.; Wang, B.; Feng, X. Covalent organic frameworks with record pore apertures. *J. Am. Chem. Soc.* **2022**, *144*, 5145−5154.

(2) Zuo, X.; Zhu, C.; Xian, W.; Meng, Q. W.; Guo, Q.; Zhu, X.; Wang, S.; Wang, Y.; Ma, S.; Sun, Q. Thermo-osmotic energy conversion enabled by covalent-organic-framework membranes with record output power density. *Angew. Chem., Int. Ed.* **2022**, *61*, No. e202116910.

(3) Sheng, F.; Wu, B.; Li, X.; Xu, T.; Shehzad, M. A.; Wang, X.; Ge, L.; Wang, H.; Xu, T. Efficient ion sieving in covalent organic framework membranes with sub-2-nanometer channels. *Adv. Mater.* **2021**, *33*, No. 2104404.

(4) Kandambeth, S.; Dey, K.; Banerjee, R. Covalent organic frameworks: chemistry beyond the structure. *J. Am. Chem. Soc.* **2019**, *141*, 1807−1822.

(5) Wang, Z.; Yang, Y.; Zhao, Z.; Zhang, P.; Zhang, Y.; Liu, J.; Ma, S.; Cheng, P.; Chen, Y.; Zhang, Z. Green synthesis of olefin-linked covalent organic frameworks for hydrogen fuel cell applications. *Nat. Commun.* **2021**, *12*, No. 1982.

(6) Koh, J. X.; Geng, K.; Jiang, D. Smart covalent organic frameworks: dual channel sensors for acids and bases. *Chem. Commun.* **2021**, *57*, 9418−9421.

(7) Wang, X.; Shi, B.; Yang, H.; Guan, J.; Liang, X.; Fan, C.; You, X.; Wang, Y.; Zhang, Z.; Wu, H.; Cheng, T.; Zhang, R.; Jiang, Z. Assembling covalent organic framework membranes with superior ion exchange capacity. *Nat. Commun.* **2022**, *13*, No. 1020.

(8) Wang, M.; Zhang, P.; Liang, X.; Zhao, J.; Liu, Y.; Cao, Y.; Wang, H.; Chen, Y.; Zhang, Z.; Pan, F.; Zhang, Z.; Jiang, Z. Ultrafast seawater desalination with covalent organic framework membranes. *Nat. Sustain.* **2022**, *5*, 518−526.

(9) He, G.; Zhang, R.; Jiang, Z. Engineering covalent organic framework membranes. *Acc. Mater. Res.* **2021**, *2*, 630−643.

(10) Mohata, S.; Dey, K.; Bhunia, S.; Thomas, N.; Gowd, E. B.; Ajithkumar, T. G.; Reddy, C. M.; Banerjee, R. Dual nanomechanics in anisotropic porous covalent organic framework janus-type thin films. *J. Am. Chem. Soc.* **2022**, *144*, 400−409.

(11) Cao, L.; Chen, I. C.; Chen, C.; Shinde, D. B.; Liu, X.; Li, Z.; Zhou, Z.; Zhang, Y.; Han, Y.; Lai, Z. Giant osmotic energy conversion through vertical-aligned ion-permselective nanochannels in covalent organic framework membranes. *J. Am. Chem. Soc.* **2022**, *144*, 12400−12409.

(12) Yuan, J.; You, X.; Khan, N. A.; Li, R.; Zhang, R.; Shen, J.; Cao, L.; Long, M.; Liu, Y.; Xu, Z.; Wu, H.; Jiang, Z. Photo-tailored heterocrystalline covalent organic framework membranes for organics separation. *Nat. Commun.* **2022**, *13*, No. 3826.

(13) Liu, R.; Tan, K. T.; Gong, Y.; Chen, Y.; Li, Z.; Xie, S.; He, T.; Lu, Z.; Yang, H.; Jiang, D. Covalent organic frameworks: an ideal platform for designing ordered materials and advanced applications. *Chem. Soc. Rev.* **2021**, *50*, 120−242.

(14) Cao, L.; Liu, X.; Shinde, D. B.; Chen, C.; Chen, I. C.; Li, Z.; Zhou, Z.; Yang, Z.; Han, Y.; Lai, Z. Oriented two-dimensional covalent organic framework membranes with high ion flux and smart gating nanofluidic transport. *Angew. Chem., Int. Ed.* **2022**, *61*, No. e202113141.

(15) Zhan, G.; Cai, Z. F.; Strutynski, K.; Yu, L.; Herrmann, N.; Martinez-Abadia, M.; Melle-Franco, M.; Mateo-Alonso, A.; Feyter, S. Observing polymerization in 2D dynamic covalent polymers. *Nature* **2022**, *603*, 835−840.

(16) Hao, Q.; Zhao, C.; Sun, B.; Lu, C.; Liu, J.; Liu, M.; Wan, L. J.; Wang, D. Confined synthesis of two-dimensional covalent organic framework thin films within superspreading water layer. *J. Am. Chem. Soc.* **2018**, *140*, 12152−12158.
(17) Kumar Mahato, A.; Bag, S.; Sasmal, H. S.; Dey, K.; Giri, I.; Linares-Moreau, M.; Carbonell, C.; Falcaro, P.; Gowd, E. B.; Vijayaraghavan, R. K.; Banerjee, R. Crystallizing sub 10 nm covalent organic framework thin films via interfacial-residual concomitance. *J. Am. Chem. Soc.* **2021**, *143*, 20916−20926.
(18) Fan, Y.; Wen, Q.; Zhan, T. G.; Qi, Q. Y.; Xu, J. Q.; Zhao, X. A case study on the influence of substitutes on interlayer stacking of 2D covalent organic frameworks. *Chem. - Eur. J.* **2017**, *23*, 5668−5672.
(19) Ascherl, L.; Sick, T.; Margraf, J. T.; Lapidus, S. H.; Calik, M.; Hettstedt, C.; Karaghiosoff, K.; Döblinger, M.; Clark, T.; Chapman, K. W.; Auras, F.; Bein, T. Molecular docking sites designed for the generation of highly crystalline covalent organic frameworks. *Nat. Chem.* **2016**, *8*, 310−316.
(20) Ying, Y.; Tong, M.; Ning, S.; Ravi, S. K.; Peh, S. B.; Tan, S. C.; Pennycook, S. J.; Zhao, D. Ultrathin two-dimensional membranes assembled by ionic covalent organic nanosheets with reduced apertures for gas separation. *J. Am. Chem. Soc.* **2020**, *142*, 4472−4480.
(21) Yang, R.; Liu, S.; Sun, Q.; Liao, Q.; Xi, K.; Su, B. Potential Difference-Modulated Synthesis of Self-Standing Covalent Organic Framework Membranes at Liquid/Liquid Interfaces. *J. Am. Chem. Soc.* **2022**, *144*, 11778−11787.
(22) Jiang, S. Y.; Gan, S. X.; Zhang, X.; Li, H.; Qi, Q. Y.; Cui, F. Z.; Lu, J.; Zhao, X. Aminal-linked covalent organic frameworks through condensation of secondary amine with aldehyde. *J. Am. Chem. Soc.* **2019**, *141*, 14981−14986.
(23) Dey, K.; Mohata, S.; Banerjee, R. Covalent organic frameworks and supramolecular nano-synthesis. *ACS Nano* **2021**, *15*, 12723−12740.
(24) Koner, K.; Karak, S.; Kandambeth, S.; Karak, S.; Thomas, N.; Leanza, L.; Perego, C.; Pesce, L.; Capelli, R.; Moun, M.; Bhakar, M.; Ajithkumar, T. G.; Pavan, G. M.; Banerjee, R. Porous covalent organic nanotubes and their assembly in loops and toroids. *Nat. Chem.* **2022**, *14*, 507−514.
(25) Feriante, C. H.; Jhulki, S.; Evans, A. M.; Dasari, R. R.; Slicker, K.; Dichtel, W. R.; Marder, S. R. Rapid synthesis of high surface area imine-linked 2D covalent organic frameworks by avoiding pore collapse during isolation. *Adv. Mater.* **2020**, *32*, No. e1905776.
(26) Kang, C.; Zhang, Z.; Wee, V.; Usadi, A. K.; Calabro, D. C.; Baugh, L. S.; Wang, S.; Wang, Y.; Zhao, D. Interlayer shifting in two-dimensional covalent organic frameworks. *J. Am. Chem. Soc.* **2020**, *142*, 12995−13002.
(27) Chao, L.; Niu, T.; Gao, W.; Ran, C.; Song, L.; Chen, Y.; Huang, W. Solvent engineering of the precursor solution toward large-area production of perovskite solar cells. *Adv. Mater.* **2021**, *33*, No. 2005410.
(28) Yin, J.; Yao, X.; Liou, J.-Y.; Sun, W.; Sun, Y.-S.; Wang, Y. Membranes with highly ordered straight nanopores by selective swelling of fast perpendicularly aligned block copolymers. *ACS Nano* **2013**, *7*, 9961−9974.
(29) Sun, W.; Wang, Z.; Yao, X.; Guo, L.; Chen, X.; Wang, Y. Surface-active isoporous membranes nondestructively derived from perpendicularly aligned block copolymers for size-selective separation. *J. Membr. Sci.* **2014**, *466*, 229−237.
(30) Zhao, X.; Liu, T.; Kaplan, A. B.; Yao, C.; Loo, Y. L. Accessing highly oriented two-dimensional perovskite films via solvent-vapor annealing for efficient and stable solar cells. *Nano Lett.* **2020**, *20*, 8880−8889.
(31) Jeon, N. J.; Noh, J. H.; Kim, Y. C.; Yang, W. S.; Ryu, S.; Seok, S. I. Solvent engineering for high-performance inorganic-organic hybrid perovskite solar cells. *Nat. Mater.* **2014**, *13*, 897−903.
(32) Min, J.; Jiao, X.; Ata, I.; Osvet, A.; Ameri, T.; Bäuerle, P.; Ade, H.; Brabec, C. J. Time-dependent morphology evolution of solution-processed small molecule solar cells during solvent vapor annealing. *Adv. Energy Mater.* **2016**, *6*, No. 1502579.
(33) Zhang, Q.; Matsuoka, F.; Suh, H. S.; Beaucage, P. A.; Xiong, S.; Smilgies, D.-M.; Tan, K. W.; Werner, J. G.; Nealey, P. F.; Wiesner, U. B. Pathways to mesoporous resin/carbon thin films with alternating gyroid morphology. *ACS Nano* **2018**, *12*, 347−358.
(34) Zhang, M.; Li, Y.; Yuan, W.; Guo, X.; Bai, C.; Zou, Y.; Long, H.; Qi, Y.; Li, S.; Tao, G.; Xia, C.; Ma, L. Construction of flexible amine-linked covalent organic frameworks by catalysis and reduction of formic acid via the eschweiler-clarke reaction. *Angew. Chem., Int. Ed.* **2021**, *60*, 12396−12405.
(35) Wang, M.; Wang, Y.; Zhao, J.; Zou, J.; Liang, X.; Zhu, Z.; Zhu, J.; Wang, H.; Wang, Y.; Pan, F.; Jiang, Z. Electrochemical interfacial polymerization toward ultrathin COF membranes for brine desalination. *Angew. Chem., Int. Ed.* **2023**, *62*, No. e202219084.
(36) Weast, R. *CRC Handbook of Chemistry and Physics*, 58th ed.; Taylor & Francis: Boca Raton, 1977; pp E55−E57.
(37) Xiao, A.; Zhang, Z.; Shi, X.; Wang, Y. Enabling covalent organic framework nanofilms for molecular separation: Perforated polymer-assisted transfer. *ACS Appl. Mater. Interfaces* **2019**, *11*, 44783−44791.
(38) Xiao, A.; Shi, X.; Zhang, Z.; Yin, C.; Xiong, S.; Wang, Y. Secondary growth of bi-layered covalent organic framework nanofilms with offset channels for desalination. *J. Membr. Sci.* **2021**, *624*, No. 119122.
(39) Wang, Y. Nondestructive creation of ordered nanopores by selective swelling of block copolymers: Toward homoporous membranes. *Acc. Chem. Res.* **2016**, *49*, 1401−1408.
(40) Tan, Z.; Chen, S.; Peng, X.; Zhang, L.; Gao, C. Polyamide membranes with nanoscale Turing structures for water purification. *Science* **2018**, *360*, 518−521.
(41) Liang, Y.; Zhu, Y.; Liu, C.; Lee, K. R.; Hung, W. S.; Wang, Z.; Li, Y.; Elimelech, M.; Jin, J.; Lin, S. Polyamide nanofiltration membrane with highly uniform sub-nanometre pores for sub-1 Å precision separation. *Nat. Commun.* **2020**, *11*, No. 2015.
(42) Pendse, A.; Cetindag, S.; Lin, M. H.; Rackovic, A.; Debbarma, R.; Almassi, S.; Chaplin, B. P.; Berry, V.; Shan, J. W.; Kim, S. Charged layered boron nitride-nanoflake membranes for efficient ion separation and water purification. *Small* **2019**, *15*, No. e1904590.
(43) Wu, M. B.; Yang, F.; Yang, J.; Zhong, Q.; Korstgen, V.; Yang, P.; Muller-Buschbaum, P.; Xu, Z. K. Lysozyme membranes promoted by hydrophobic substrates for ultrafast and precise organic solvent nanofiltration. *Nano Lett.* **2020**, *20*, 8760−8767.
(44) Kandambeth, S.; Biswal, B. P.; Chaudhari, H. D.; Rout, K. C.; Kunjattu, H. S.; Mitra, S.; Karak, S.; Das, A.; Mukherjee, R.; Kharul, U. K.; Banerjee, R. Selective molecular sieving in self-standing porous covalent-organic-framework membranes. *Adv. Mater.* **2017**, *29*, No. 1603945.
(45) Chen, L.; Hu, B.; Zhang, J.; Zhang, J.; Huang, S.; Ren, P.; Zou, Y.; Ding, F.; Liu, X.; Li, H. A facile synthesis of 1,3,6,8-pyrenesulfonic acid tetrasodium salt as a hydrosoluble fluorescent ink for anti-counterfeiting applications. *RSC Adv.* **2019**, *9*, 476−481.
(46) Jiao, L.; Zhang, M.; Li, H. Preparation of 1, 3, 6, 8-pyrenesulfonic acid tetrasodium salt dye-doped silica nanoparticles and their application in water-based anti-counterfeit ink. *Materials* **2020**, *13*, No. 4074.

https://doi.org/10.1021/jacs.3c03198
J. Am. Chem. Soc. 2023, 145, 11431−11439